Effect of Riblets Geometry on Drag Reduction

Dr. Ikhlase M. Fayed* & Dr. Nibras M. Mahdi*

Received on:20/4/2010
Accepted on:5/8/2010

Abstract

The effect of longitudinal riblet surface models (U, V and semi-Circular and U with fillet corner riblets) on the performance of unsymmetrical airfoil (NACA23015) which has been investigated numerically and experimentally. Numerical investigation involve examining drag reduction by solving the governing equations (Continuity and Navier-Stokes equations) using the known package FLUENT version (6.1) in turbulent regime with appropriate turbulence model (κ-ε). Also measurement in experimental work will be carried out. The results indicate that the riblet surface models are the key parameters for controlling the boundary layer characteristic. The most effective riblet surface is U-riblet with fillet model (Mo.4, h=0.1mm), by compare to smooth model, the results show a small increment in lift slope curve about (9%) and total drag decrease (12%) over the angles of attack range from (0° to 17°).

Keywords: Drag reduction, Riblets, Airfoils.

تأثير شكل الحزوز على تخفيض الكبح

الخلاصة

يتناول البحث تاثير الحزوز الطوليه (U ، V ، نصف دائره وU ذات زاوية محدبة) على أداء جناح ذو المقطع غير المتناظر (NACA23015) عددياً وعملياً. البحث العددي يتضمن حل المعادلات الحاكمة (معادلات الأستمرارية ونافير-ستوكس) لدراسة امكانية تخفيض الكبح باستخدام برنامج (FLUEN6.1) في نظام اضطرابي مع نموذج الأضطراب (κ-ε). وكذلك أجريت القياسات في العمل المختبري. النتائج بينت ان انواع الحزوز هي عامل مهم في السيطرة على خصائص الطبقة المتاخمة والنموذج الأكثر فعالية هو النموذج U مع زاوية محدبة (Mo.4, h=0.1mm) بالمقارنة مع النموذج الأملس، حيث بينت النتائج زيادة صغيرة في منحني الرفع (9%) وانخفاض في الكبح الكلي (12%) لمدى من زوايا الهجوم (0° الى 17°).

1.0 Introduction

Biological surfaces exhibit structures which are, at first sight, both appealing and enigmatic, as shown in figure (1). In particular, the skin surfaces of aquatic animals interesting fluid-dynamic effects, these surface structures only unfold under the microscope. Some of the concepts which seem to be used by nature remain tough scientific problems and are only partly understood, one such example is the compliant skin of sharks or dolphins. The story started with "Gray's paradox", Bechert, et al 2000 suggested there was a huge gap between the speed of the shark and its available (estimated) physiological power to achieve this speed. It has been assumed that dolphin skin would also work under fully turbulent flow conditions. The expected effects are skin friction reduction of only a few percent. The skin friction drag plays a major role in the overall efficiency of aircraft, high speed vehicles, marine vessels

* Machines & Equipments Engineering Department, University of Technology/ Baghdad

and piping and ducting systems. The skin friction is part of the resistance that the object encounters when moving in the fluid. For instance, in case of an airplane, up to (50%) of the total resistance is due to skin friction, Houghton and Carpenter 2003. In order to save energy, it is profitable to try and keep skin friction as low as possible, Bechert, et al 2000. In the following, some possible mechanisms will be described in order to reduce skin friction in a turbulent boundary layer.

The studies in the generated turbulent boundary layer during the turbulent flow contain different vortices in intensity and size. These vortices play important role in the dissipation kinetic energy for stream fluid through turbulence generation from vortices. The researchers found that the longitudinal vortices (inner region of turbulent boundary layer) extends with flow direction and contains a fluid that has low velocity (compare with free stream velocity) and its vortices face series explosion that generate new turbulence during the boundary layer. The generated shear stress above the surface is related with vortices intensity. Therefore a lot of researchers take care when trying to look at the effect of vortices by changing the nature of flow that uses the riblet in order to reduce the friction drag generated during the turbulent flow.

Walsh 1983 examined the drag characteristics of longitudinally ribbed surfaces. Direct drag measurements are presented for V-riblet, and larger wavelength transverse curvature riblets (h^+<25 and s^+<30). The direct drag data indicate net drag reductions as (8%) for certain V-riblet with heights in terms of law of the wall coordinates (h^+=10 and s^+=15). Where, Rzuqe 1988 studied the effect of riblet on the drag reduction. The riblets was in the form of an adhesive tape of various thickness (h^+=6.5, 13 and 19.5), width (wo^+=93 and 186) and spacing (s^+=93 and 186) lined parallel to the flow direction. Result has show that certain manipulated surfaces reduce the drag force by about (10%), with riblet having dimension (h^+=6.5, s^+=186 and wo^+=93), but the other surfaces generally increase the drag. Also, Benhalilou and Anselmet in 1994 carried out measurements for both mean and turbulent dynamic fields over a semi-circular riblet wall with (h^+=17 and s^+=34). The turbulent kinetic energy (k^+), deduced from the three velocity standard deviations, is strongly increased above the rib ridge, and reduced over the valley. A similar effect is also visible on the Reynolds stress ($-u'v'$) profiles. The Reynolds shear stress are seen to be larger and more frequent above the riblet than over the smooth wall, whereas they are reduced above the valley. Comparison of the respective productions of turbulence above a riblet and above smooth walls, inferred at the distance (y^+=9) above the ridge plane, indicates a reduction of about (5%) in the manipulated flow. Bernal 1997 performed an experimental work for a flat plate with V-riblets. Riblets with (s/h =1) and (s =1.83 mm) was tested using a free stream velocity of (2.5m/s). It was found that nearly (6%) of drag reduction achieved. The turbulent intensity profile for the riblets case is lower than without them, and the maximum value was reported for (y^+=13). Turbulent energy of the spectra with riblets was found to be

reduced compared to the energy spectra without riblets and the turbulent intensity with riblets is lower than without them and the maximum value is achieved about (y^+≈10.9). Raju and Viswanath 1998 carried out an experimental work in a low speeds wind tunnel on a (13.6%) thick GAW(2) airfoil model, (trailing edge thickness ratio of (0.5%)) with V-riblet films a height of (0.076 and 0.152 mm) were used; they were applied between (0.1 and 0.96*c*) on both the top and bottom surface. The total drag was determined from the Pitot and static measurements in the wake; a constant temperature hot wire anemometer was used to assess the existence of vortex shedding behind the base. The results further show that the drag reduction is maintained up to an airfoil incidence of (6˚) and it is only about (7%). Indinger, et al in 2004 examined the influence of riblet on the attached and separated flow. Two types of surface were investigated: a smooth surface and a surface with semi-circular riblet (*h*/*s*=0.5) aligned in main flow direction. Particle image velocimetry was used to determine the influence of the surface structure on large scale structures in the near wall region whereas profiles of mean and fluctuating velocity inside the boundary layer were acquired by laser Doppler anemometry. They found significant changes of size and location of near wall vortex structures ongoing with a deformation of the mean velocity profile due to the riblet surface.

The aim of investigation are preparing generation geometry and a mathematical model convenient to study the effect of riblet and riblet geometry (U, V and semi-Circular riblet) on aerodynamic characteristic of a cambered airfoil NACA23015. This includes choosing an appropriate turbulence model by using the known package FLUENT version (6.1) to solve the problem numerically. Experiment simulation, airfoil model NACA23015 with different U-riblet surface were fabricated with different riblet heights (*h*=0.1, 0.15, 0.2 and 0.25mm). To investigate the problem experimentally, open circuit low speed wind tunnel was used. Measurement devices were used to obtain velocity and velocity fluctuating on streamwise and also to measure direct lift and drag forces acting on the wing models.

2.0 Theoretical Model and Numerical Solution

In order to analyze the flow field around airfoils with smooth and different riblet surfaces, a solution of Navier- stokes equations is required.

The analyzes of flow field around airfoil (NACA23015) with and without riblet surfaces, using a governing partial differential equation in three dimensions which are based on conservation of mass and momentum equations. To demonstrate the effect of the turbulence on the flow, turbulence model that involves the solution of two transport equation (k-ε) model is used. Thus numerical techniques have to solve these equations using finite volume in Cartesian coordinates system (x,y,z). Where, the working fluid is air and the flow characteristics are steady state, Newtonian fluid, incompressible and turbulent flow.

2.1 Riblet Models Geometry

The geometry of U, V, Semi-Circular and U riblet with fillet

corner models will be presented in table (1), Nibras 2009.

2.2 Governing Partial Differential Equations (PDE)

The time averaged steady-state conservation equation for continuity, momentum of turbulent flow can be written in a Cartesian coordinate as follows, Cebeci and Smith 1974:

(I) Continuity Equation:

$$\frac{\partial U}{\partial x}+\frac{\partial V}{\partial y}+\frac{\partial W}{\partial z}=0 \quad \text{.....} \quad \text{.....(1)}$$

(II) Momentum Equations:

X-Momentum Equation

$$\frac{\partial U^2}{\partial x}+\frac{\partial UV}{\partial y}+\frac{\partial UW}{\partial z}=-\frac{1}{r}\frac{\partial P}{\partial x}+\frac{\partial}{\partial x}\left(u\frac{\partial U}{\partial x}\right)+\frac{\partial}{\partial y}\left(u\frac{\partial U}{\partial y}\right)+\frac{\partial}{\partial z}\left(u\frac{\partial U}{\partial z}\right)+\frac{\partial}{\partial x}\left(-\overline{u'^2}\right)+\frac{\partial}{\partial y}\left(-\overline{u'v'}\right)+\frac{\partial}{\partial z}\left(-\overline{u'w'}\right) \quad \text{.....(2)}$$

Y-Momentum Equation

$$\frac{\partial UV}{\partial x}+\frac{\partial V^2}{\partial y}+\frac{\partial VW}{\partial z}=-\frac{1}{r}\frac{\partial P}{\partial y}+\frac{\partial}{\partial x}\left(u\frac{\partial V}{\partial x}\right)+\frac{\partial}{\partial y}\left(u\frac{\partial V}{\partial y}\right)+\frac{\partial}{\partial z}\left(u\frac{\partial V}{\partial z}\right)+\frac{\partial}{\partial x}\left(-\overline{u'v'}\right)+\frac{\partial}{\partial y}\left(-\overline{v'^2}\right)+\frac{\partial}{\partial z}\left(-\overline{v'w'}\right) \quad \text{.....(3)}$$

Z-Momentum Equation

$$\frac{\partial UW}{\partial x}+\frac{\partial VW}{\partial y}+\frac{\partial W^2}{\partial z}=-\frac{1}{\rho}\frac{\partial P}{\partial z}+\frac{\partial}{\partial x}\left(\upsilon\frac{\partial W}{\partial x}\right)+\frac{\partial}{\partial y}\left(\upsilon\frac{\partial W}{\partial y}\right)+\frac{\partial}{\partial z}\left(\upsilon\frac{\partial W}{\partial z}\right)+\frac{\partial}{\partial x}\left(-\overline{u'w'}\right)+\frac{\partial}{\partial y}\left(-\overline{v'w'}\right)+\frac{\partial}{\partial z}\left(-\overline{w'^2}\right) \quad \text{.....(4)}$$

2.3 Turbulence Model (k-ε)

The standard (k-ε) model has two model equations one for (k) and the other for (ε), which can be formulated as follows, Pulliam 1994:

$$\frac{\partial}{\partial x}(kU)+\frac{\partial}{\partial y}(kV)+\frac{\partial}{\partial z}(kW)=\frac{\partial}{\partial x}\left(\frac{u_t}{s_k}\frac{\partial k}{\partial x}\right)+\frac{\partial}{\partial y}\left(\frac{u_t}{s_k}\frac{\partial k}{\partial y}\right)+\frac{\partial}{\partial z}\left(\frac{u_t}{s_k}\frac{\partial k}{\partial y}\right)+G-e \quad \text{.....} \quad (5)$$

$$\frac{\partial}{\partial x}(eU)+\frac{\partial}{\partial y}(eV)+\frac{\partial}{\partial z}(ew)=\frac{\partial}{\partial x}\left(\frac{u_t}{s_e}\frac{\partial e}{\partial x}\right)+\frac{\partial}{\partial y}\left(\frac{u_t}{s_e}\frac{\partial e}{\partial y}\right)+\frac{\partial}{\partial z}\left(\frac{u_t}{s_e}\frac{\partial e}{\partial z}\right)+C_{1e}\frac{e}{k}G-C_{2e}\frac{e^2}{k} \quad \text{...(6)}$$

$$G=u_t\left[2\left(\frac{\partial U}{\partial x}\right)^2+2\left(\frac{\partial V}{\partial y}\right)^2+2\left(\frac{\partial W}{\partial z}\right)^2+\left(\frac{\partial V}{\partial x}+\frac{\partial U}{\partial y}\right)^2+\left(\frac{\partial V}{\partial z}+\frac{\partial W}{\partial x}\right)^2+\left(\frac{\partial V}{\partial z}+\frac{\partial W}{\partial y}\right)^2\right] \quad \text{.....(7)}$$

Where; $n_t=C_m\frac{k^2}{e}$

e: is the dissipation term.

The empirical constants appearing in the above equations that are achieved at by comprehensive fitting data for a wide range of turbulent flows are expressed as follows in table (2).

2.4 The Boundary Conduction at The Wall

There are five types of input boundary condition at the wall for the present work:

- Free stream ($u = u_\infty$),
- No Slip (u, v, w, k, $\varepsilon = 0$) at the wall
- At the upper limit of the computational domain $\partial / \partial y = 0$
- On the lateral boundaries ($z = 0$, $z = s/2$), $\partial / \partial z = 0$
- All velocity components specified at the upper boundary are periodic in spanwise location (z). The cyclic (periodic boundary condition) for riblet on Straight Wing, as shown in figure

(2), which can be applied for unsymmetric airfoil, any Angle of attack and any Type of riblet.

2.5 Numerical Approach by Fluent

To perform simulations of these systems (such as the airflow around an aircraft) on a computer, these PDEs need to be discretised, resulting in a finite number of points in space at which variables such as velocity, pressure are calculated. The usual methods of discretisation, such as finite volumes, use neighboring points to calculate derivatives, and so there is the concept of a mesh or grid on which the computation is performed. The main type of PDE used is elliptic, which is suitable for domains with closed boundaries (for unbounded domains, a fictitious boundary at large distances is used), which is used in the CFD part of the present work.

The simplest grid generation technique is the algebraic method which is used in the FLUENT 6.1 for the present work. Two dimensional C and rectangular grids, so named because of their approximate shape, are slight extensions of the simple 'rectangular' block, C and H grid elements with multi-block are used in the present work, details about the grid generation and solution of equations are described by Nibras 2009. The computational blocks are usually simple rectangles, but corners in the computational space need not correspond to corners in the physical space and vice versa, figure (3), Filipiak 1996. At these degenerate points, care needs to be taken with the difference formulation. But cuts can be made to transform them to simply-connected blocks that can transfer map to a rectangle, and this leads to the C and rectangular grids. The grid close to the trailing edge of the airfoil should also be adequately clustered. A grid-sensitivity has been done to investigate the effect of grid spacing near the trailing edge on the lift coefficient. It is found that a spacing of (0.001) of the chord length between the trailing edge point and the first point in the wake is needed to correctly capture the high lift over the airfoil. The grid size is (200×50×60 nodes) with physical domain (12*c* upstream and 20*c* downstream). Airfoil mesh illustrated in figure (3) and all riblets cross section type are meshed with structured mesh, as shown in figure (4).

It should be mentioned here that the dimensions (span and chord) of the airfoil model used at the computational domain and the experimental tests are the same for the present work. The input data for the software were the atmospheric air properties with Reynolds number value based on the chord of (3.56×10^5).

2.6 Aerodynamic Characteristics

Application of momentum conservation laws shows that the forces and moments on an airfoil are due to two sources:

1. Pressure distribution on the surface of the airfoil, and
2. Shear stress distribution over the surface of the airfoil.

The relations between these forces and the pressure and stress distribution in terms of non-dimensional coefficients are given by, Houghton and Carpenter, 2003:

$$C_n = \frac{1}{c}\left[\int_0^c \left(Cp_l - Cp_u\right)dx + \int_o^c \left(Cf_u \frac{dy_u}{dx} - Cf_l \frac{dy_l}{dx}\right)dx\right] \quad ....(8)$$

$$C_a = \frac{1}{c}\left[\int_o^c \left(Cp_u \frac{dy_u}{dx} - Cp_l \frac{dy_l}{dx}\right) dx + \int_0^c \left(Cf_u - Cf_l\right)dx\right] \quad ....(9)$$

Where, the pressure coefficient and the shear stress coefficients are given as:

$$Cp = \frac{P - P_\infty}{\frac{1}{2} r u_\infty^2} \quad , \quad Cf = \frac{t}{\frac{1}{2} r u_\infty^2} \quad ...(10)$$

So, the lift coefficient and drag coefficient are related by:

$$Cl = C_n \cos a - C_a \sin a \quad .....(11a)$$

$$Cd = C_n \sin a + C_a \cos a \quad .....(11b)$$

3.0 Experimental Facilities

The experiments were performed in an open circuit type, low speed wind tunnel (Plint & Partners LTD.) at University of Technology as shown in figure (5). The test section is (610 mm long, 305 mm wide, and 305 mm height) in which airfoil was mounted horizontally to span the test section. The top and side walls of test section were made from Perspex (Plexiglas) for operational and giving full visibility. At the upstream end of the test section there is a static tapping. The pressure probes can be traversed in streamwise and vertical direction through (380 mm long, 9 mm wide slot) at the ceiling of the test section. The operating velocity is adjustable from (4 to 35m/s) was controlled by means of a double butterfly valve at the fan outlet.

Mean velocity of air at the test section was (32.25m/s), the Reynolds number based on the mean velocity and airfoil chord length was (3.56×10^5). Flow uniformity was verified by measuring the velocity distribution, using a standard Pitot-static tube, between the floor and ceiling at the inlet to the test section and at the middle (340 mm from the test section inlet) as shown in figure (5). Boundary layer thickness on smooth and riblet surfaces can be measured by flat pitot tube, (with such this probe the error of order of (0.05mm)). The probe and associated pressure measuring equipment have a long time lag because of the small flow passage (0.0254 mm) at the probe tips, Chue 1975. The hot wire anemometer has been applied to the measurement of moving air currents and fluctuations in the velocity.

3.1 Riblet Models

Brass plates (source) (Gauge40) have been used, it is mounting in rotating machine. Put amount of sensitive substance (Resists) above plate then close and operate the machine for a period of time. Stop the machine (it will be dry by heater). Now, the plate is ready for printing. Put the film (design) on the plate under vacuum pressure, then will be transfer to the grove machine which operate under light source. Waiting approximate 15 to 30 minutes (when the plate receives the light more than (30 minutes) the print operation will be more accuracy), in this time the film is printing on the plate. Putting a plate in a container having a boil blue ink, moving the container from the left to the right until the design will appear.

The plate is washing in pure water and leave it to dry, prepare a fixed substance (yellow color (Fixer)), which is fixing to the first sensitive substance (Resists), at the same time while the plate has been written in the blue ink, the container was moving left and right for a

period of time. Pull out the plate and wash it by pure water, until dry from water. The plate has been maintained and exposure to heat for moment and moving it until the color change from yellow to black or brown. Leave it with a period to cold with coating the back of the plate by color. In the front of plate that has the design, cut and close (correct) any thing out of the design for remain the design is clean. When the operating (correcting) has been finished, the plate merged on a container having a solution of the grove substance (Fe_2Cl_2) and water. Moving the container left and right for period (15 to 30 minuets) until the design has been grooved. The plate is cleaning by THANER to remove the sensitive substance. Putting the plate in container has a boil hydrochloric acid (HCl) (Batsh) to clean the printing and pull out the plate. The design has been grooved, figure (6). The results plate groove models and dimensions from manufactur in Table 3 and figure (7).

3.2 Airfoil Models

Airfoil section (NACA23015) is used in the present test, the model is made from mahogany wood, it used for pressure measurement in wind tunnel with chord length (150mm) and span length (303mm), figure (8). A transition trip-wire of (0.8 mm) diameter was fixed at (x/c=0.06) on the upper surface, Raju and Viswanath 1998.

4.0 Results and Discussion

Numerical and experimental investigations are reported and will be discussed in this section, for a turbulent, incompressible, steady flow over smooth and riblet surface models for airfoil (NACA23015).

Figure (9) present the near riblet velocity and vorticity contours for representing of the three families of riblets considered. In all cases, very steep velocity gradients occur around the crest of the riblet, it is this feature which makes the performance of the U- riblet profile so sensitive to the riblet thickness even though there is a negligible effect on the flow within the valley itself. Note also that the velocity contours increase for circular and V-riblet through cross section more than that for the U-riblet. This is why it achieves the poorest drag reduction performance.

As streamwise vortices in the viscous sublayer approach the riblet, the riblet peak starts shedding vortictiy of opposite sign. This is due to the spanwise cross flow generated by the vortices and the accompanying separation at the riblet tips. This causes the existence of secondary vortices (so the behavior of flow around the riblet is characterized by fluctuation). These secondary vortices are associated with a strong momentum mixing in the riblet valleys whereas low momentum fluid is washed out of the valleys and high momentum fluid is pumped into the valleys. This could mean that killing the secondary vortices or decreasing their strength would be a step in the direction of more drag reduction. The generation of secondary vortices at the riblet peaks serves two functions; first, weakening of the streamwise vortices that generate the secondary vortices and second the retention of low speed fluid within the riblet.

The center location of the vortices is obtained by finding the position with maximum vorticity value. From vorticity distribution contours as shown in figure (9) it can be seen that the vorticity center is concentrated near the riblet tips.

(This may be attributed to the secondary vortex induced by the riblet tip effect) for models circular and V- riblet while addition vortices exist at mid valley of riblet U- riblet model. The streamwise vortices and the secondary vortices induced by the riblet tip are distorted and have an elongated shape inside the riblet valley.

Figure (10) show the turbulent kinetic energy distribution for the U-riblet surface model (Mo.1) for NACA23015 at different angle of attack and sketch the effect of model (Mo.1) on smooth model with angle of attack ($\alpha=0^{\circ}$ and 10°). These results ensure the fact of energize the boundary layer by controlling the sublayer region and it will be more effective. It was found that the turbulent kinetic energy will be reduced with riblet compared to the kinetic energy without riblet, about (15%) for NACA23015 (at $x/c=0.8$ and $\alpha=0^{\circ}$) as presented in figure (10).

Measured surface chordwise pressure distribution for NACA23015 at angles of attack ($\alpha=0^{\circ}$-10°) with and without riblet models (Mo.4, 5, 6 and 7) are presented in figures (11-12). The chordwise pressure distribution on the riblet surface for two models (Mo.4 and 7) are quit different from that on smooth surface.

Pressure area distribution with riblet surface is larger than smooth surface due to inflows towards the wall carry high streamwise momentum and, when reaching smooth wall, spread laterally. This creates an extended area of the surface with high streamwise velocity gradient. The impact of inflow can lead to an increase in the pressure at smooth wall and, with riblet (impede lateral motion of the inrush at the wall), this is often present only in the riblet immediately below the inflow. So the size of region with high streamwise velocity gradient is then decreased. The larger area with riblet will result in a substantial contribution to the lift, U-riblet with model (Mo.4) has larger area for all measurement.

Figure (13) show the alteration of the mean velocity profile due to riblet of model (Mo.4) (measured at $x/c=0.2$, 0.5 and 0.8) at angle of attack ($\alpha=5^{\circ}$ and 10°) for NACA23015. The mean velocity in the presence of riblet is slightly fuller away from the wall (less full boundary layer profile), more effective in adverse pressure gradient at ($x/c=0.8$) which implied a decrease in the value of displacement and momentum thickness, as shown in below table and figure (14). However the velocity gradient at the surface for the flow over the riblet surface is lower than value for the smooth surface.

Reduction in aerodynamic characteristic of U-riblet model (Mo.4) with respect to smooth model at ($x/c=0.5$) as:

Aerodynamic Characteristic	NACA23015
Velocity Profile	26%
Displacement thickness	29%
Momentum thickness	32%

It can be seen in figure (14), that the wall shear stress in the valleys is generally less than the wall shear stress at a smooth wall, indicating small velocity gradients in the valleys. A traverse from riblet tip through the valley up to neighboring tip is important, it is seen near the tips, the wall shear stress due to riblet

is higher than the average smooth wall friction coefficient due to strong secondary vortices at tip that have mechanism for the transport high downstream momentum fluid into the riblet valley. When traversing from the tips via the midpoint to the valleys however, it is found that the friction quit rapidly decreases to level lower than this average due to the absence of the fluctuation in the riblet valleys and the Reynolds stress is indeed small there. This is an indication of the fact that the amount of momentum mixing is small in the valley. The reduction in wall shear stress is (25% for semi-circular riblet, 40% for V-riblet and 45% for U-riblet) than smooth surface at ($Re=3.56\times10^5$ and $\alpha=0^\circ$). The shear stress for semi-circular and V-riblet surfaces increases (100%, 110% respectively) with an increase angle of attack except for the U- riblet model that has small increase about (22%). The best geometry of the three kind of riblet airfoil surface models (U, V and semi-circular riblet) is U-riblet (Mo.1), which is extended to full study in the experimental work by taking another models with different dimension (Mo.4, 5, 6 and 7).

The history of the lift and drag coefficient with the angle of attack is shown in figure (15). The results in the case of smooth surface and those for riblet surface models are presented. The effective riblet surface is U-riblet model (Mo.4) (h=0.1 mm), where the increase in lift coefficient as compared with the smooth surface exceeds (9%) for NACA23015, and decrease in drag coefficient about (12%) for NACA23015 at angle of attacks (5°-10°). One can conclude that, by applying the riblet surfaces for the flow at the shear layer instability frequency "the double advantages" that is the higher lift and less drag. This in turn ensures the enhancement performance of the present riblet surfaces. Also one can notice that the favorite behavior is at angles of attack ($\alpha=5^\circ$-10°).

Results of percentage total drag reduction ($\Delta Cd/Cds$) for different riblet models at each (α), are shown in figure (16) for NACA23015. The observation was suggestive that drag reduction due to riblets can increase up to an angle of attack (5°) then decreases gradually with increasing angle of attack, where U-riblet model (Mo.4) has shown the greatest drag reduction. The percentage of total drag reduction for NACA23015 increased initially with angle of attack from about (8%) at ($\alpha=0^\circ$) to (12%) at ($\alpha=5^\circ$) then decrease to (9%) at ($\alpha=17^\circ$). At higher angle of attack ($\alpha>5^\circ$) drag reduction fell gradually due to the progressing deceleration of the upper surface boundary leading eventually to separation.

5.0 Conclusions

The study of results of the riblet surfaces effect on aerodynamic characteristics of wing models showed the increase in lift about (9%) and decrease in drag about (12%) caused by riblet surfaces model, the riblet model (Mo.1, h=0.1mm) has significant improvement. The slope of (Cl increase and decrease in Cd) obviously results from reduced boundary layer displacement thickness distribution caused by riblets; essentially riblets lead to a lower drag effect on the airfoil. The results also showed that Cl(max) angle of attack and the corresponding stall angle were unaffected by riblets. The (Cl/Cd)

ratio increase initially with ($\alpha = 0^{\circ}$) to maximum increase in ($\alpha = 10^{\circ}$). The adverse pressure gradient on the airfoil upper surface was a dominated factor resulting in increased drag reduction.

References

[1] Bechert W., Bruse M. and Meyer R, "Fluid mechanics of biological surfaces and technological application", Turbulence research dep., Institute of propulsion technology, German aerospace center, Naturwissen schaften 87:157–171, Springer, 2000.

[2] Benhalilou M. and Anselmet F., "Conditional reynolds stress on a V-Groove surface", Institut de mecanique de marseill, France, Phys Fluids 6 (6), 1994.

[3] Bernal J. J., "Micro bubble drag reduction, phenomenon study in a channel flow", Texas A & M University, Ph. D. Theses, 1997.

[4] Cebeci T. and Smith O., "Analysis of turbulent boundary layers", ACADEMIC Press, INC. 1974.

[5] Chue S. H., "Pressure probes for fluid measurement", Progress in aerospace sciences, Vol. 16, No.2, pp. 147-223, 1975.

[6] Filipiak M., "Mesh generation", Edinburgh parallel computing centre, The university of edinburgh, technology watch report, 1996.

[7] Houghton L. and Carpenter W., "Aerodynamics for engineering students", 5th Edition, University of warwick, Heinemann An imprint of elsevier science, 2003.

[8] Indinger T., Hickel S. and Adams N., "3D measurements in an adverse pressure gradient turbulent boundary layer over smooth and ribbed surface", Technisch university, German, 2004.

[9] Nibras M., "Effect of riblets geometry on drag reduction and its application on airfoils", Mech. Eng. Dep., UOT, Ph.D Theses, 2009.

[10] Pulliam T. , "Solution methods in computational fluid dynamics", Research scientist ames center, von k'arm'an institute for fluid mechanics, Belgium, 1994.

[11] Raju C. and Viswanath P., "Base drag reduction caused by riblets on GAW(2) airfoil", National aerospace lab., India, AIAA, Vol.35, No.6, 1998.

[12] Rzuqe M. H., "Drag reduction in fluid flow by using longitudinal ribs", Mechanical rng. dep., UOT, M. Sc. Theses, 1988.

[13] Walsh M. J., "Riblets as a viscous drag reduction technique", NASA langley research center, Virginia, AIAA, Vol.21, 1983.

Table (1) Riblet shape models description.

Riblet shape	Height, *h* (mm	Pitch, *s* (mm)	Riblet model
U- Riblet	**0.1**	**0.2**	**Mo.1**
V- Riblet	**0.1**	**0.2**	**Mo.2**
Semi-Circular Riblet	**0.1**	**0.25**	**Mo.3**
U- Riblet with fillet corner	**0.1**	**0.4**	**Mo.4**
U- Riblet with fillet corner	**0.15**	**0.5**	**Mo.5**
U- Riblet with fillet corner	**0.2**	**0.6**	**Mo.6**
U- Riblet with fillet corner	**0.25**	**0.65**	**Mo.7**

Table (2) Empirical constants in the *k-e*, Pulliam 1994

C_m	C_{1e}	C_{2e}	s_k	s_e
0.09	*1.44*	*1.92*	*1.00*	*1.30*

Table (3) Riblet Plate models and dimension

Riblet Plate Dimension			P_W mm	P_L mm	P_H mm
			300	200	0.4
Model	h mm	t mm	w mm	s mm	r mm
Mo.4	0.1	0.3	0.1	0.4	0.02
Mo.5	0.15	0.35	0.15	0.5	0.02
Mo.6	0.2	0.4	0.2	0.6	0.02
Mo.7	0.25	0.4	0.25	0.65	0.02

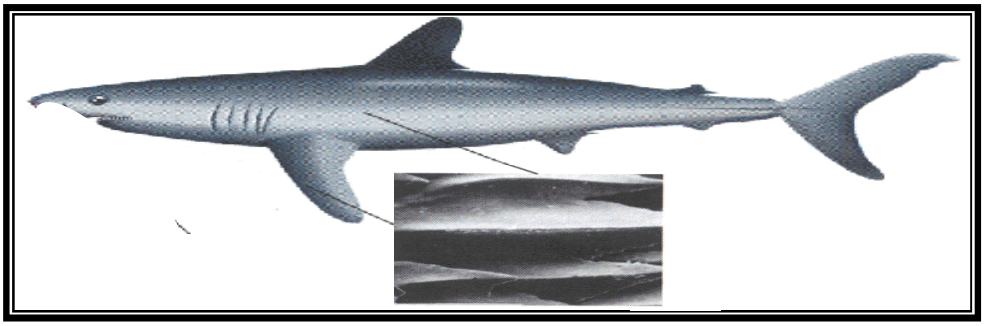

Figure (1) Biological surfaces (shark skin photo), Bechert, et al 2000.

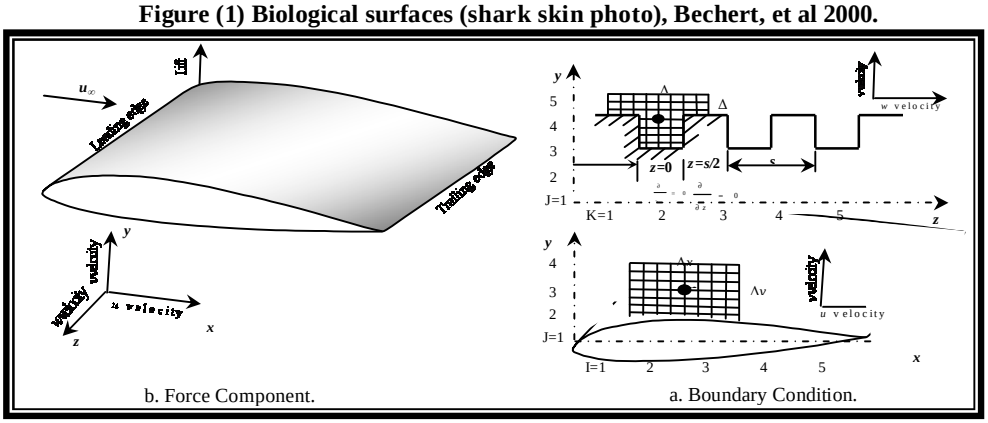

b. Force Component. a. Boundary Condition.

Figure (2) The boundary condition and the force components

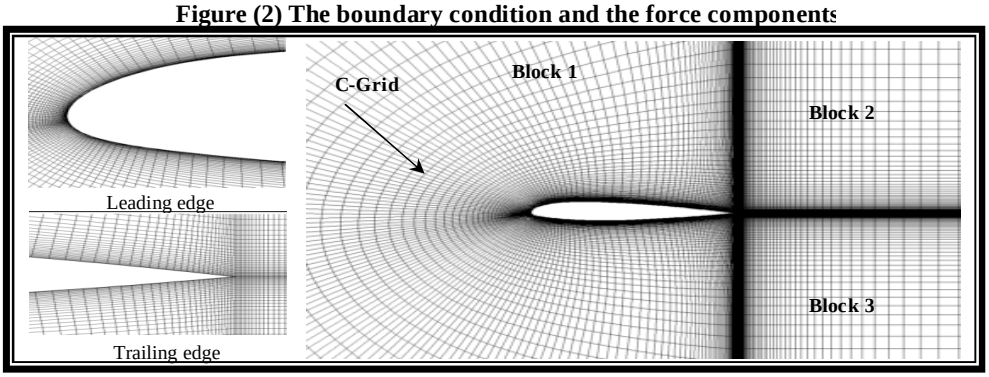

Figure (3) Mesh grid around airfoil

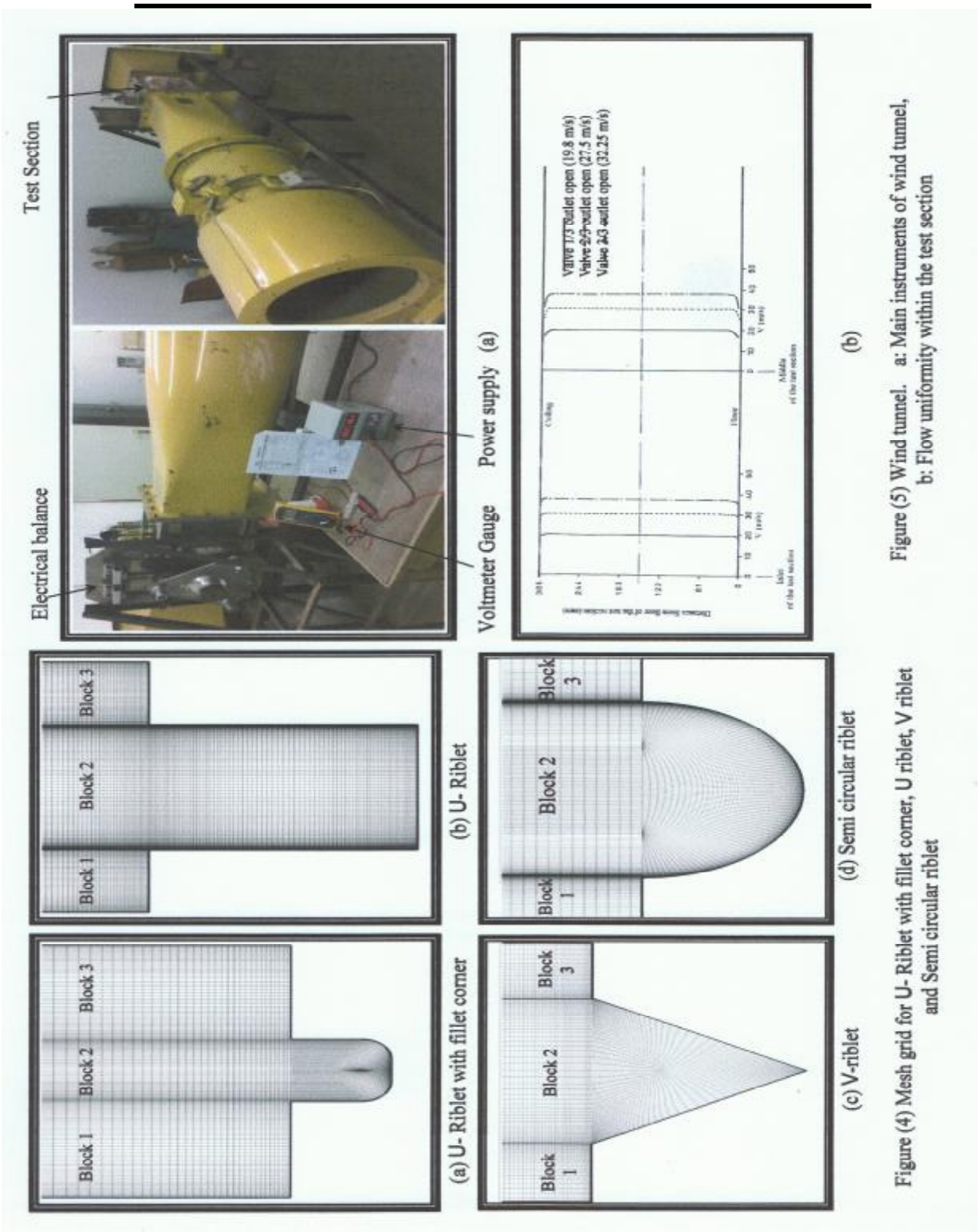

Figure (5) Wind tunnel. a: Main instruments of wind tunnel, b: Flow uniformity within the test section

Figure (4) Mesh grid for U- Riblet with fillet corner, U riblet, V riblet and Semi circular riblet

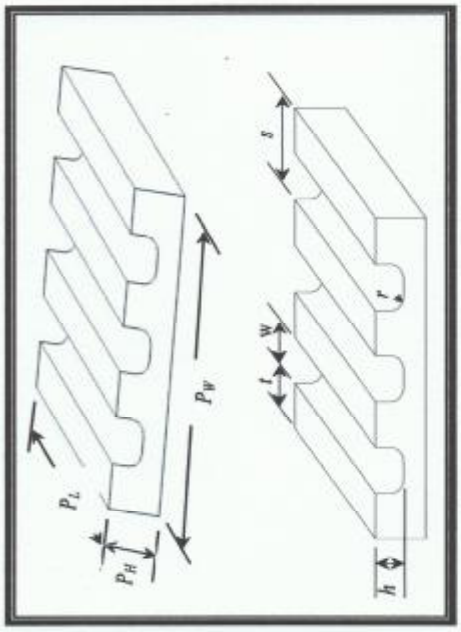

Figure (7) Riblet plate model description

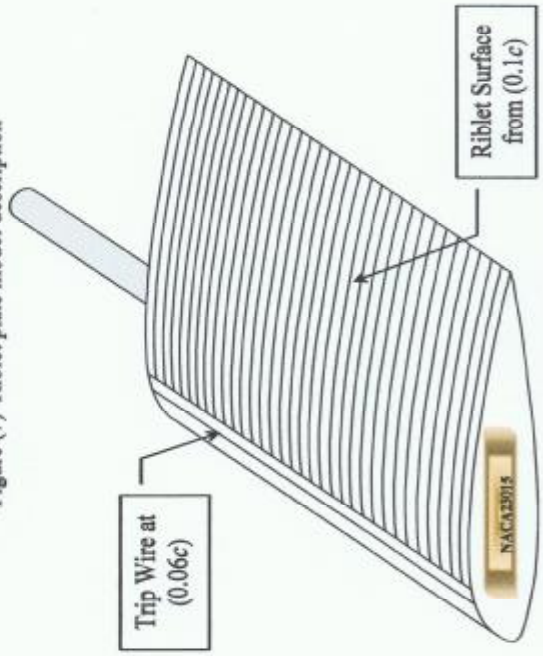

Figure (8) Wing (NACA23015) model layout

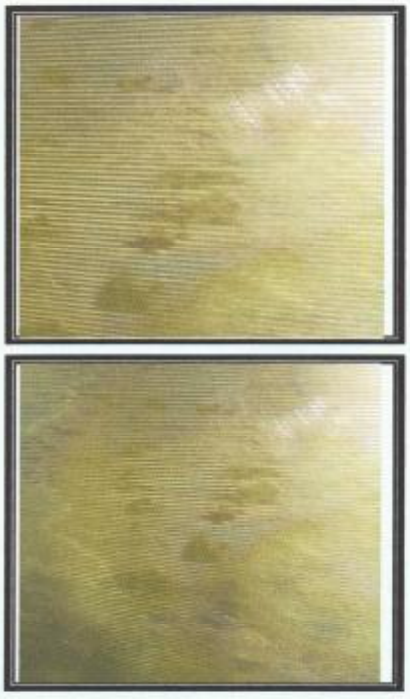

a: Model (Mo.4) (h=0.1mm) b: Model (Mo.5) (h=0.15mm)

c: Model (Mo.6) (h=0.2mm) d: Model (Mo.7) (h=0.25mm)

Figure (6) Riblet brass plate manufacturing.

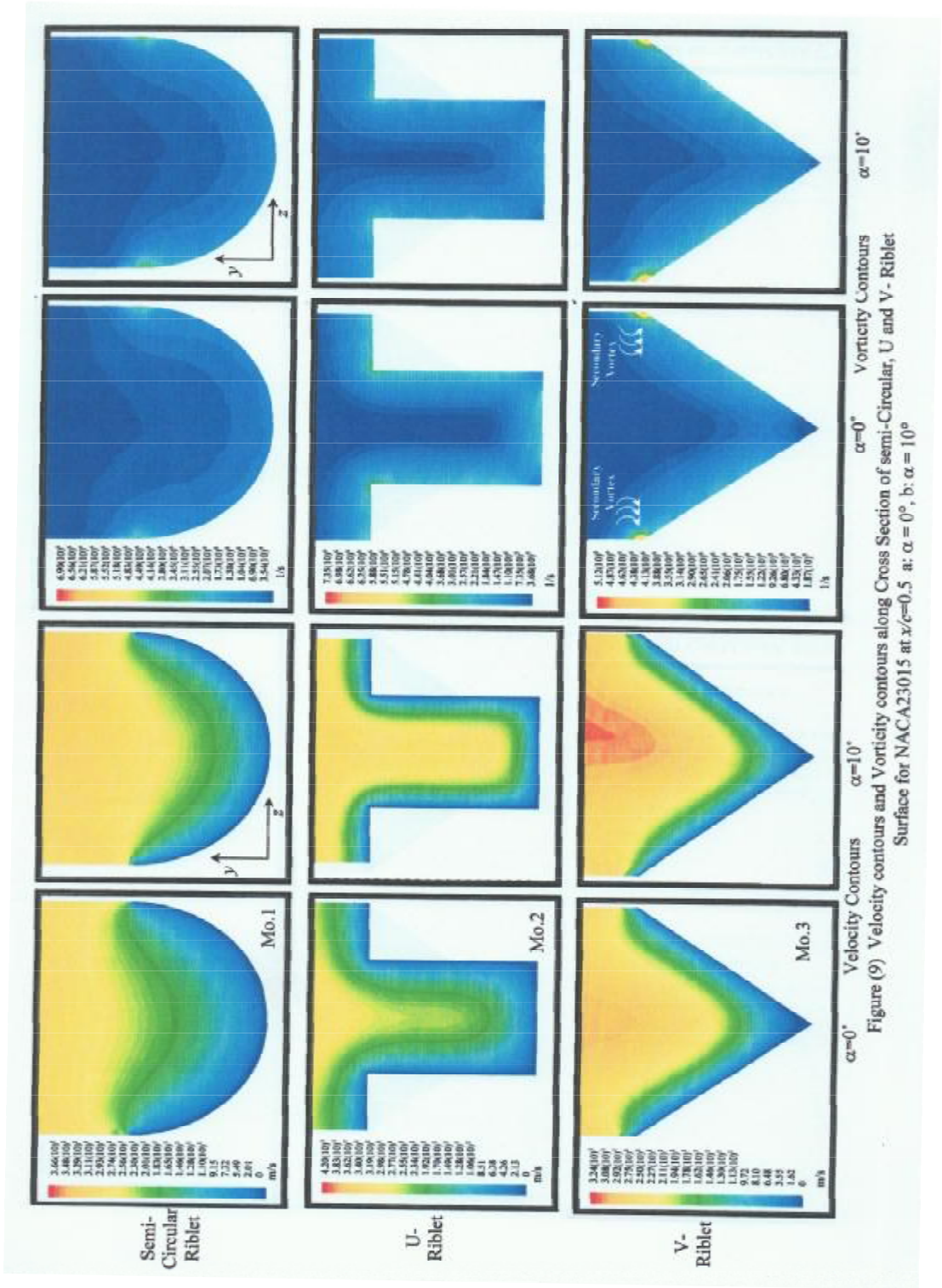

Figure (9) Velocity contours and Vorticity contours along Cross Section of semi-Circular, U and V- Riblet Surface for NACA23015 at x/c=0.5 a: $\alpha = 0°$, b: $\alpha = 10°$

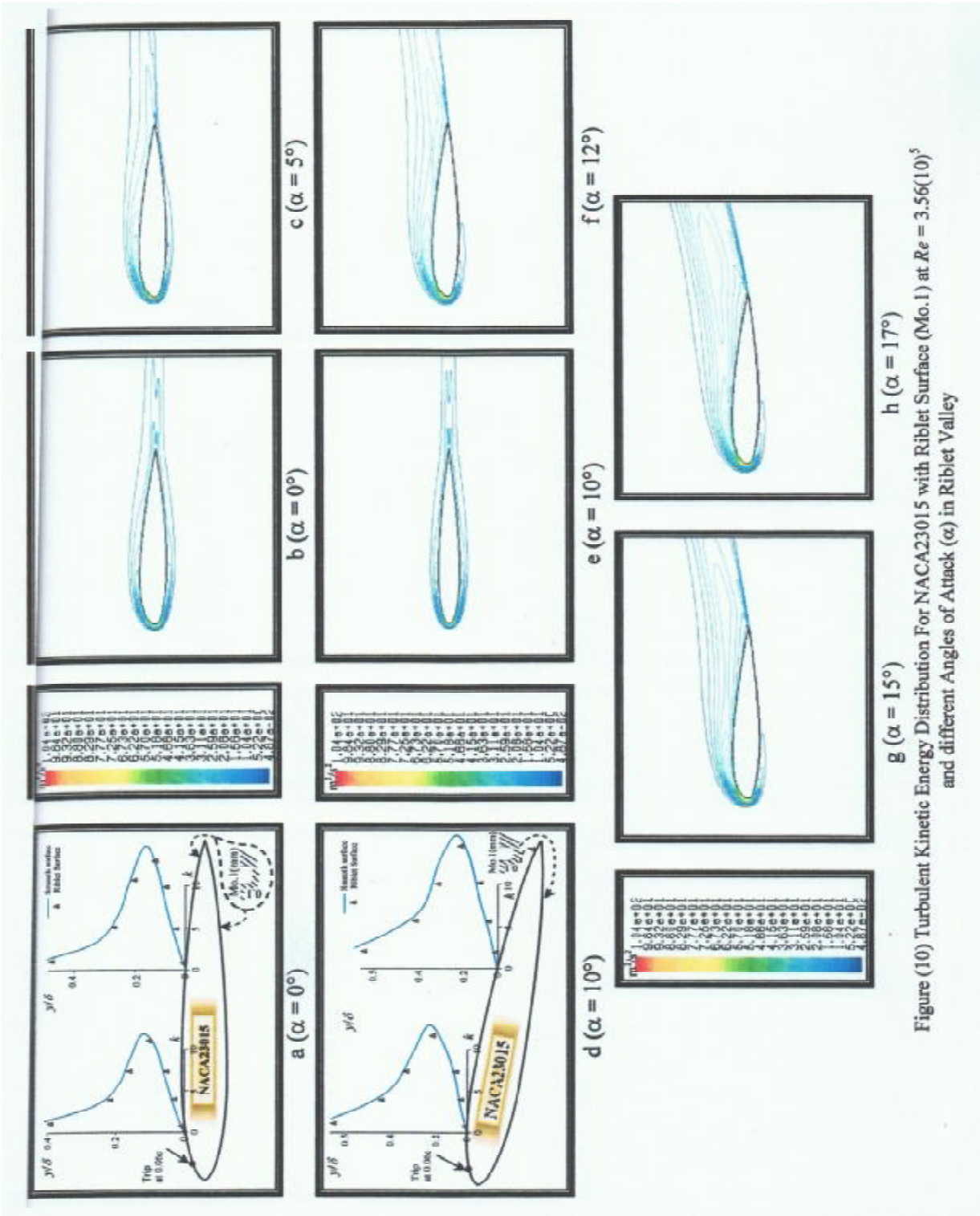

Figure (10) Turbulent Kinetic Energy Distribution For NACA23015 with Riblet Surface (Mo.1) at $Re = 3.56(10)^5$ and different Angles of Attack (α) in Riblet Valley

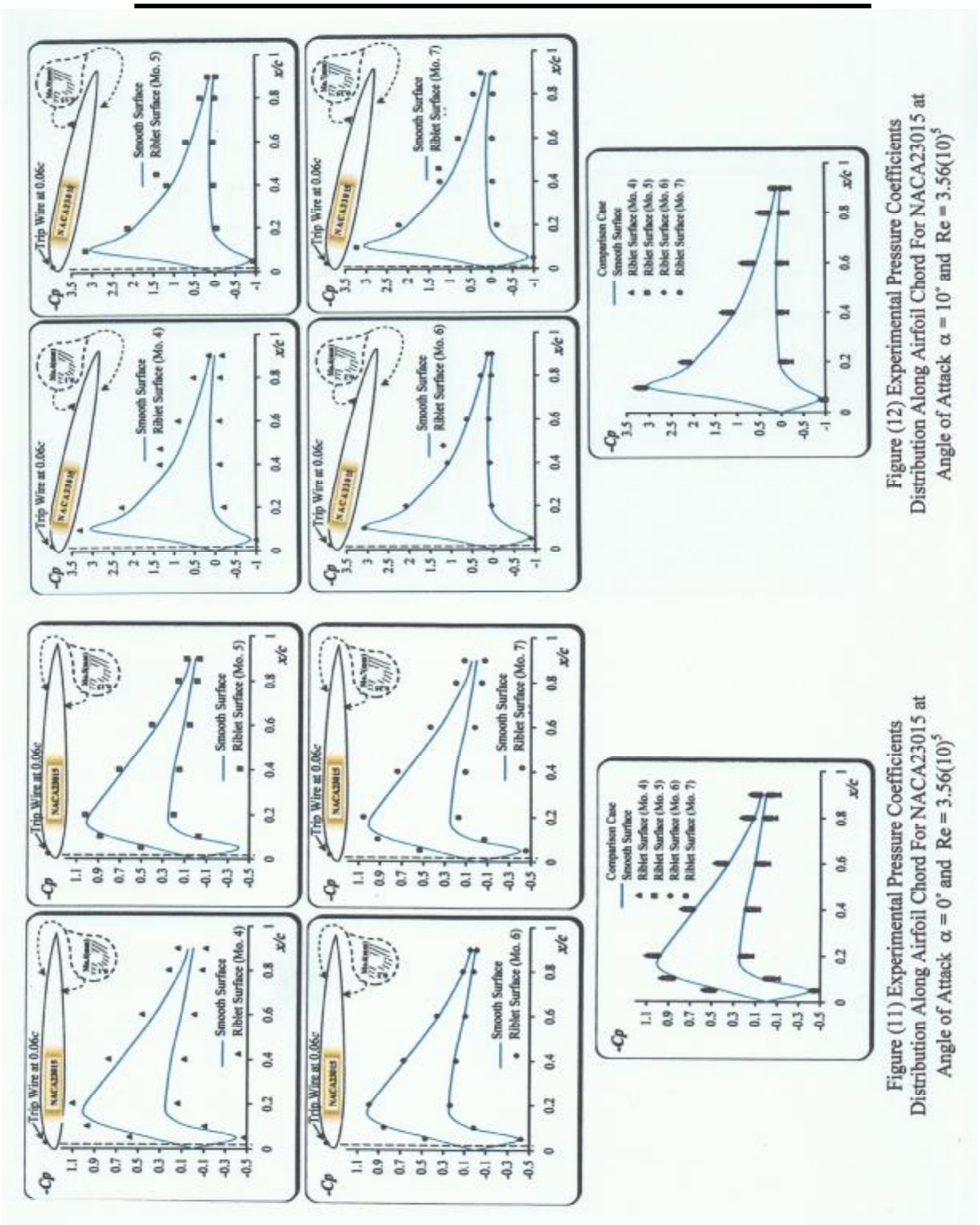

Figure (11) Experimental Pressure Coefficients Distribution Along Airfoil Chord For NACA23015 at Angle of Attack $\alpha = 0°$ and $Re = 3.56(10)^5$

Figure (12) Experimental Pressure Coefficients Distribution Along Airfoil Chord For NACA23015 at Angle of Attack $\alpha = 10°$ and $Re = 3.56(10)^5$

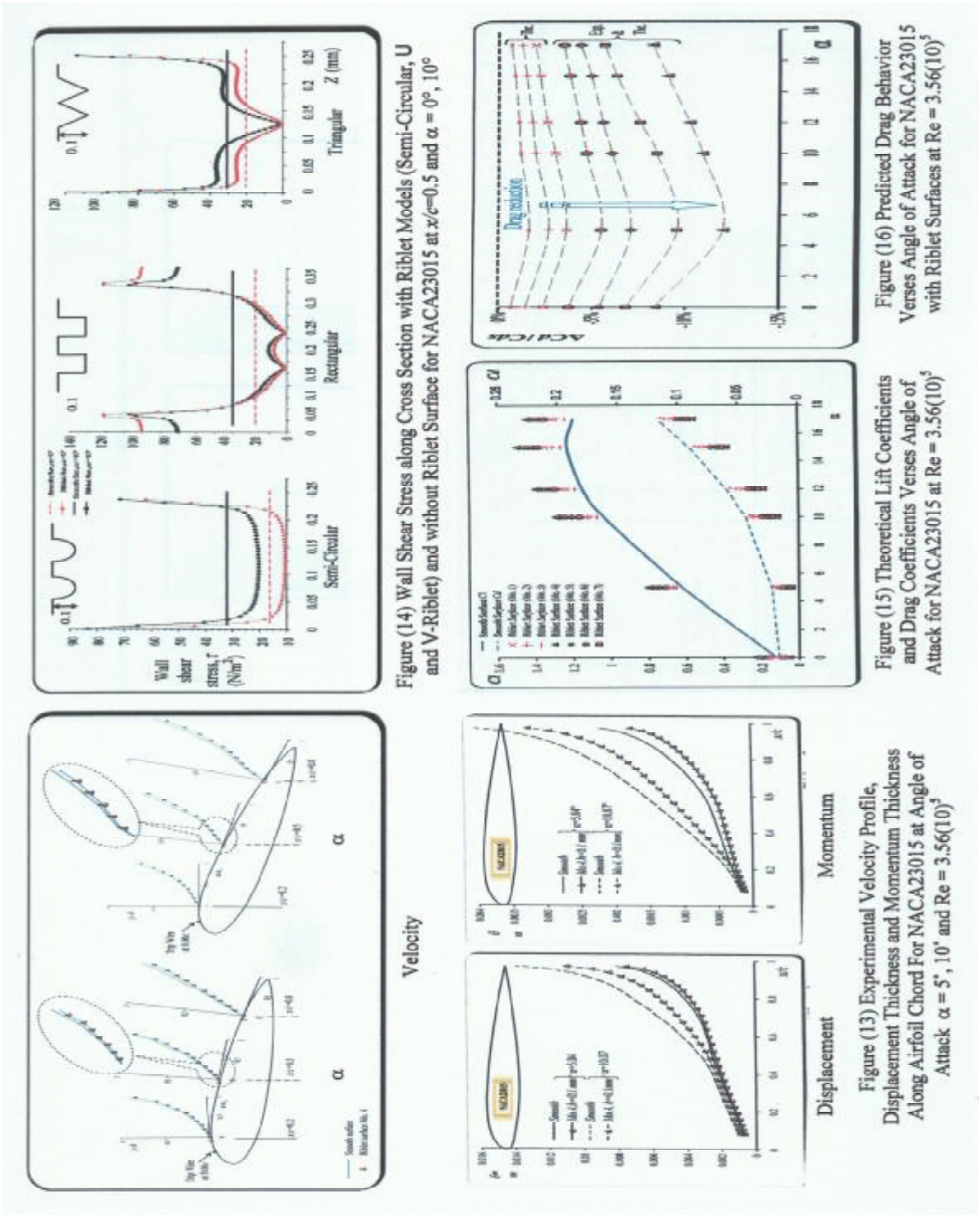

Figure (14) Wall Shear Stress along Cross Section with Riblet Models (Semi-Circular, U and V-Riblet) and without Riblet Surface for NACA23015 at x/c=0.5 and α = 0°, 10°

Figure (16) Predicted Drag Behavior Verses Angle of Attack for NACA23015 with Riblet Surfaces at Re = 3.56(10)^5

Figure (15) Theoretical Lift Coefficients and Drag Coefficients Verses Angle of Attack for NACA23015 at Re = 3.56(10)^5

Figure (13) Experimental Velocity Profile, Displacement Thickness and Momentum Thickness Along Airfoil Chord For NACA23015 at Angle of Attack α = 5°, 10° and Re = 3.56(10)^5

Nomenclature

Character	Description	Units	Character	Description	Units
c	Chord Length	m	s^+	Riblet width Scaled with Friction Velocity	----
C_a	Axial Force Coefficient	----	t	Spanwise along plate grooved	m
Cd	Drag Coefficient	----	U, V, W	Mean Velocity Components	m/s
Cf	Skin Friction Coefficient	----	u,v,w	Cartesian Velocity Components	m/s
Cl	Lift Coefficient	----	u_∞	Free-Stream Velocity	m/s
Cp	Pressure Coefficient	----	u', v', w'	Reynold Stress	m^2/s^2
C_n	Normal Force Coefficient	----	w	Riblet Width	m
$C_m, C_{e1}, C_{e2}, s_k, s_e$	Constants in $k-e$ Model	1/s	w^+	Spanwize Velocity Component Scaled with Friction Velocity	----
h	Riblet Groove Height	m	w_o^+	Riblet Width Scaled with Friction Velocity	----
h^+	Riblet Height Scaled with Friction Velocity	----	x, y, z	Cartesian Coordinate	m
k	Turbulent Kinetic Energy	m^2/s^2	**Greek Symbols**		
k^+	Kinetic Energy Scaled with Friction Velocity	----	a	Angle of Attack	degree
P	Pressure	N/m^2	Δ	Boundary layer thickness	m
P_H	Plate Grooved Height	m	e	Dissipation of Turbulent Kinetic Energy	m^2/s^2
P_W	Plate Grooved Width	m	υ	Kinematics Viscosity	m^2/s
P_L	Plate Grooved Length	m	υ_e	Effective Kinematics Viscosity	m^2/s
Re	Reynolds Number	----	υ_t	Eddy Kinematics Viscosity	m^2/s
r	Radius of Riblet Filet	m	r	Density of Air	kg/m^3
s	Riblet Pitch	m	t	Shear Stress	N/m^2